Femtosecond spectroscopy

2001 J. Phys.: Condens. Matter 13 7873

(http://iopscience.iop.org/0953-8984/13/34/325)

INSTITUTE OF PHYSICS PUBLISHING JOURNAL OF PHYSICS: CONDENSED MATTER

J. Phys.: Condens. Matter **13** (2001) 7873–7884 PII: S0953-8984(01)26618-1

Femtosecond spectroscopy

S Link, H A Dürr and W Eberhardt

Institut für Festkörperforschung, Forschungszentrum Jülich, 52425 Jülich, Germany

Received 6 July 2001
Published 9 August 2001
Online at stacks.iop.org/JPhysCM/13/7873

Abstract

The development of femtosecond laser systems has opened the door to studying ultrafast dynamical processes, which range from nuclear motion in molecules to relaxation mechanisms of charge carriers in solids. A characteristic of the approach is that the system investigated is no longer in thermodynamic equilibrium. It is rather in an excited state whose decay into other degrees of freedom is being probed. We will, in this article, outline the general experimental set-up needed for such studies and discuss typical experiments involving excited electrons in solids.

1. Introduction

Electronic relaxation in solids happens on fs and ps timescales [1, 2]. It is instructive to try to visualize this order of magnitude. The speed of light in vacuum is about 300 000 km s^{-1}. This implies that a light pulse circles the Earth about 7.5 times each second. In one nanosecond the same light pulse traverses only 30 cm. Typically fs laser pulses are about 100 fs long (currently the shortest pulse is 4.5 fs [3]). Such pulses are, therefore, about 30 μm long. This represents the positional accuracy of optical elements that is required in a so-called pump–probe experiment. A pump laser pulse drives the system investigated out of thermodynamical equilibrium. A second time-delayed probe pulse subsequently monitors the decay of this excited state. The whole process is repeated stroboscopically many times. In the following we will discuss the required experimental set-up and describe two examples of electronic relaxation measurements on semiconductors and metals.

2. Experimental set-up for generating fs laser pulses

2.1. The fs laser system

We start the description of the laser system with a short introduction to laser technology. Three important components for the optical resonator of any laser are a mirror with 100% reflectivity, a laser medium and an output coupler with a reflectivity <100%. Light amplification is only possible if the gain of the laser medium exceeds the losses inside the resonator. In general

this condition is only fulfilled for a small wavelength range depending on the laser medium used. In addition, the light path L inside the resonator determines the number of modes with wavelengths λ which could be amplified:

$$L = m\frac{\lambda}{2} \qquad m = 1, 2, 3, \ldots \tag{1}$$

where m is an integer. Wavelengths which satisfy equation (1) are referred to as longitudinal modes.

We now turn to the general requirements for the formation of ultrashort laser pulses. According to Heisenberg's uncertainty principle, the pulse length and bandwidth of the laser pulse are intimately connected. This means that the pulse length is proportional to the reciprocal bandwidth. Using the relation $\lambda = c/\nu$, the difference in frequency of two adjacent modes according to equation (1) can be written as

$$\Delta\nu = \frac{c}{2L}. \tag{2}$$

A fs pulse shorter than 100 fs which propagates through an optical resonator with $L = 1.5$ m length contains around 10^4 modes. Thus the laser medium should be able to amplify light over a wide and quasi-continuous energy range. Using Ti:sapphire (Ti:Al_2O_3) as the laser medium, this condition is fulfilled since Ti:sapphire is able to amplify light anywhere from 680 nm to 1100 nm. The coupling of up to ten adjacent modes is depicted in figure 1(a) [4]. If several modes are lasing simultaneously and they are summed with random phases, the resulting intensity distributions of the laser pulses are also random. In order to obtain a stable and well defined train of fs pulses, the phase between modes should be adjusted non-randomly and held constant as shown on the right in figure 1(a). In this case the peak powers become much larger and the random distribution between the main peaks diminishes. Figure 1(a) shows schematically that the larger the number of so-called locked modes, the higher the peak intensities and the shorter the laser pulses.

Now two questions arise: what should one do to lock thousands of modes together, and how is it possible that so many longitudinal modes operate simultaneously? Let us first answer the second question. In general the laser will operate with minor power fluctuations in a continuous-wave (cw) mode with only one or two simultaneously operating longitudinal modes. In order to increase the number of modes, a starting mechanism inside the laser cavity rapidly changes the optical length inside the cavity. This change in the cavity length terminates the previously oscillating modes, leaving atoms in the laser medium available for new modes, so there will be a period during which they can both be lasing simultaneously and power fluctuations can start. Once power fluctuations start, pulses with more or less intensity are formed. Consider an intense laser pulse with a Gaussian beam profile perpendicular to the direction of propagation. If the beam travels through matter and its light is intense enough, its electric field can distort the atoms of the material and alter the refractive index n^*. The change in n^* is large at the beam centre and decreases with increasing distance r; thus a gradient index lens is formed. Changes in the refractive index due to the beam intensity alter the beam diameter inside the cavity and the beam is narrowed. This effect of self-focusing is referred to as the optical Kerr effect. Consider now a randomly created pulse caused through power fluctuations oscillating in the cavity. This pulse travels through the Ti:sapphire crystal which acts as a Kerr lens and narrows the pulse (the shaded area on the left in figure 1(b)). Less intense power fluctuations are not able to modify the Ti:sapphire crystal, so they remain as an unnarrowed low-power background as shown on the left in figure 1(b) (shaded area). A slit aligned at the focal point in the cavity permits only the focused high-intensity pulse to pass through, while the unfocused cw background is interrupted at its edges and attenuated (on the

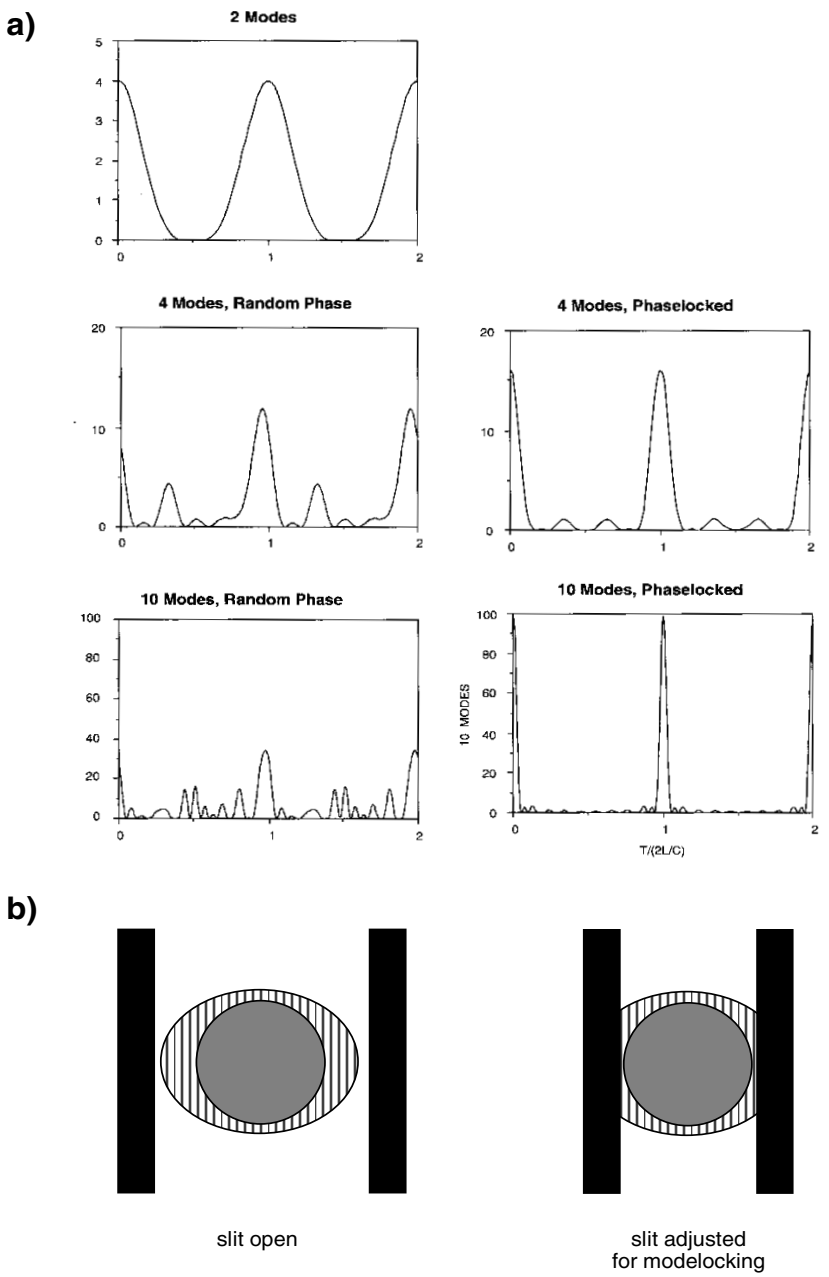

Figure 1. (a) The superposition of up to ten modes with a random (left) and a locked (right) phase distribution. If the phases are non-randomly adjusted and held constant, the peak power becomes much larger and the random spiking diminishes. (b) If the slit is open (left), both the focused, randomly created pulse and the continuous laser beam can pass through without any losses. After adjusting the slit for mode-locking operation, only the narrowed intense pulse passes through unattenuated.

right in figure 1(b)). This is the start of passive mode-locking. Since the Kerr lens is only formed upon the arrival of the intense pulse, only narrow mode-locked pulses pass through the slit unattenuated.

It can be shown that once a fs pulse is formed, the pulse lengthens after it has passed through optical elements. For instance, a 10 fs laser pulse with a centre wavelength of 795 nm is broadened to 100 fs after traversing a 1 cm thick fused silica plate [5]. This effect is well known from fundamental optics. The refractive index n^*, which determines the phase velocity of each material, depends on the wavelength λ. The first derivative $\mathrm{d}n^*(\lambda)/\mathrm{d}\lambda$ determines the group velocity and thus defines the velocity of a wavepacket with a central wavelength λ. The second derivative finally determines the group-velocity dispersion which governs the relative phase changes of the different frequency components. The material shows positive (negative) group-velocity dispersion (GVD) if the red (blue) spectral components exhibit a larger phase velocity compared to the blue (red) components. In the wavelength regime between 200 nm and 1000 nm almost all materials exhibit a positive GVD, which means that n^* increases with decreasing wavelength. As mentioned above, a fs laser pulse contains a large number of adjacent longitudinal modes. Since the different frequency components possess different phase velocities, the fs pulse is reshaped upon propagation through matter. The pulse experiences a modulation which leads to a change in frequency with time (*chirp*).

Another phenomenon affecting the fs pulse length and structure occurs when the pulse traverses the Ti:sapphire crystal. When the pulse propagates through the crystal, the refractive index is changed as a function of the light intensity and a Kerr lens is formed. The refractive index change caused is small at the leading and trailing edges, but large at the centre of the laser pulse. Thus some parts of the pulse move faster, altering the pulse shape. This effect is referred to as 'self-phase modulation' (SPM) and is equivalent to another source of positive GVD.

Since the pulse oscillates in the cavity, it receives a slight chirp from the dispersive optics (starter, wavelength tuning element, Ti:sapphire crystal) at each round-trip. In order to keep the oscillating pulse short inside the cavity, the positive GVD has to be compensated. For this purpose an optical element with negative dispersion is required. A pulse compressor inside the cavity could easily be realized using a pair of prisms as shown in figure 2 [6]. Prisms bend different wavelengths by different angles, so the pair of prisms opens up the possibility of different optical paths for different frequencies.

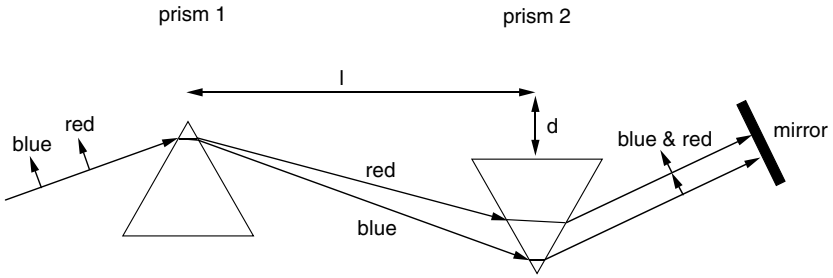

Figure 2. Chirp compensation using a pair of prisms.

The magnitude of the GVD compensation could easily be controlled by varying the distance between the two prisms or by shifting prism 2 perpendicular to its baseline. If the distance l between the two prisms is increased, the light path difference between the red and the blue parts also increases. This results in an amount of negative GVD due to the large optical path of the red part in prism 2 (optical path L = geometrical path $\times$ refractive index $= \tilde{L}n^*$). On the other hand, shifting prism 2 towards the beam increases the amount of glass in the

optical path, thus enhancing the positive GVD. Therefore the adjustable parameters l and d allow one to tune the net GVD of the cavity to zero.

The laser system used in the experiments described below consists of a Ti:Al_2O_3 oscillator (Coherent Mira Seed) and a Ti:Al_2O_3 regenerative amplifier (Coherent RegA 9000) pumped by an Ar^+ laser (Coherent Innova 400). The oscillator is tunable in a wavelength range between 780 nm and 855 nm with a bandwidth of 35 nm at a repetition rate of 76 MHz. This wavelength interval corresponds to photon energies between 1.59 eV and 1.45 eV. The restriction on the wavelength range results from the optical elements used (mirrors, tuning element) inside the cavity. If needed, the pulse can be compressed again below 50 fs using a second pair of prisms for external GVD compensation.

In order to enhance the energy per laser pulse, the output pulses from the oscillator are first stretched to a length of more than 100 ps to prevent damage to the optical elements. A regenerative amplifier (RegA) is then used for amplification by a factor of 1000 yielding a pulse energy of up to 5 μJ at a repetition rate of 250 kHz. After subsequent compression, laser pulses of 50–60 fs are available. The stretcher and compressor stages use gold-coated diffraction gratings (1200 grids per mm) instead of pairs of prisms. However, the principle of compressing or stretching the laser pulses remains the same. The corresponding power of a 50 fs laser pulse can then be calculated; it is 100 MW.

2.2. Higher-harmonic generation

Apart from alkali metals, most materials possess work functions between 4 and 6 eV; thus even in a two-photon process the laser output of around 1.5 eV is insufficient for photoemission of one electron. In order to overcome this problem, laser pulses with photon energies of up to 6 eV are required. Higher photon energies can be generated using non-linear optical processes in crystals [7]. With non-linear optical crystals such as β-barium borate (β-BBO) the infrared output can be doubled (second harmonic), tripled (third harmonic) or quadrupled (fourth harmonic). The sixth harmonic ($\approx$9 eV) can be obtained using xenon as the non-linear medium [8]. Since the conversion efficiencies especially for higher harmonics are low, a high output power of the laser system is required to provide sufficient photons per laser pulse at photon energies around 6 eV or 9 eV.

For the purpose of generating harmonics up to the sixth, in a first step the RegA output is frequency doubled using a thin ($<$1 mm) β-BBO crystal. This generates the second harmonic (blue light) with photons of around 3 eV energy. A conversion efficiency of 20–30 per cent can be obtained using a concave mirror with a 30 cm focal length as the focusing element. The choice of the second frequency conversion stage depends on the physical system under investigation.

The third harmonic with photon energies between 4.35 eV and 4.77 eV is generated by sum-frequency mixing of the fundamental and the second-harmonic radiation in a second β-BBO crystal. Since the laser pulses possess durations far below 100 fs, care has to be taken to avoid different arrival times of the 1.5 eV and 3 eV pulses at the BBO crystal. Therefore only concave mirrors rather than lenses are used to avoid a time delay between pulses of the fundamental and the second harmonic due to their different group velocities in lenses.

In order to generate the fourth harmonic, the fundamental and the second harmonic could be separated using a dichroic mirror. The second harmonic is then focused into an appropriate β-BBO crystal generating the fourth harmonic ($\approx$6 eV) via another second-harmonic process. Unfortunately, the wavelength range of the radiation generated is restricted to wavelengths $>$203 nm. The conversion efficiencies for the third and fourth harmonics are of the order of 10% and 1% [9], respectively.

The sixth harmonic can be produced at photon energies between 8.70 eV and 8.82 eV. The frequency-doubled beam is focused into a gas cell filled with xenon. The cell is separated from the UHV chamber by a MgF_2 window which is transparent for wavelengths down to 120 nm. According to phase-matching conditions, the optimal xenon pressure for the frequency-tripling process depends on the wavelength [8]. At a xenon pressure of 850 Torr a conversion efficiency of about 10^{-6} could be obtained.

2.3. Measurement of ultrashort pulses

A major ingredient in time-resolved experiments is the exact knowledge of the pulse duration at the sample [10, 11]. This has to be obtained indirectly since all direct methods fail due to the long relaxation times of common photodetectors. In order to obtain information about the pulse structure, an autocorrelation technique is usually used. In an autocorrelation set-up the beam is split into two parts of approximately equal intensity. One part is sent through a variable-optical-delay stage before both parts are recombined at the measurement point, for example at a β-BBO crystal. The superposed beam has to cause a non-linear effect, in this case second-harmonic generation or sum-frequency mixing, which is measured using a photodiode. The measured signal depends on the combined light intensity, which is a function of the time delay between the two pulses and the temporal pulse width of the laser. Since the beam is split into two parts which are subsequently combined, a correlation of the beam with itself is created, hence the name autocorrelation. The pulse structure of the infrared RegA output is monitored using such an autocorrelator with integrated spectrometer (APE pulsescope) in order to measure pulse duration and bandwidth *in situ*.

However, the monitored pulse length of the compressed RegA output is not necessarily the same as that used for pump-and-probe pulses at the sample. On the way to the sample, the beams pass through β-BBO crystals, beam splitters, lenses and the vacuum viewport. As described above, these materials exhibit GVD and therefore broaden the pulse length. In order to keep the pulses at the sample as short as possible, the grating compression stage behind the RegA amplifier is used to give the pulse a negative chirp. This is then removed by traversing the optical elements on the path to the sample.

The determination of the pulse duration at the sample can be carried out by using time-resolved two-photon photoemission (TR2PPE). Pump-and-probe pulses for a TR2PPE experiment are created by using beam splitters or, in order to separate the different harmonics, dichroic mirrors. A schematic overview for the whole optical set-up is displayed in figure 3. After the first frequency conversion stage, a beam splitter generates two pulses. The reflected part which contains 70% of the beam intensity is again frequency converted producing UV photons of around 4.5 eV or 6 eV and serves as pump pulse. The transmitted part runs through an optical delay stage (retroreflector) and serves as probe pulse. The two pulses are focused onto the sample and are brought into spatial overlap. By physically moving the retroreflector, the two pulses can be delayed in time with respect to each other. A retroreflector shift of 1 μm corresponds to a delay of 6.7 fs, so precise time-resolved measurements are possible. TR2PPE measurements have to be performed under ultrahigh-vacuum (UHV) conditions usually at a base pressure better than 6×10^{-10} mbar. For the experiments described below, electrons were detected in normal emission using a hemispherical analyser (Leybold EA200) with 100 meV energy resolution.

Figure 4 shows autocorrelation measurements of fs laser pulses using the non-linearity of the 2PPE process. Due to the intense light, each pulse causes an independent two-photon photoemission signal which is detected. During temporal overlap of individual pulses the photocurrent intensity is enhanced by a factor of 3 [12]. Consequently if the delay between

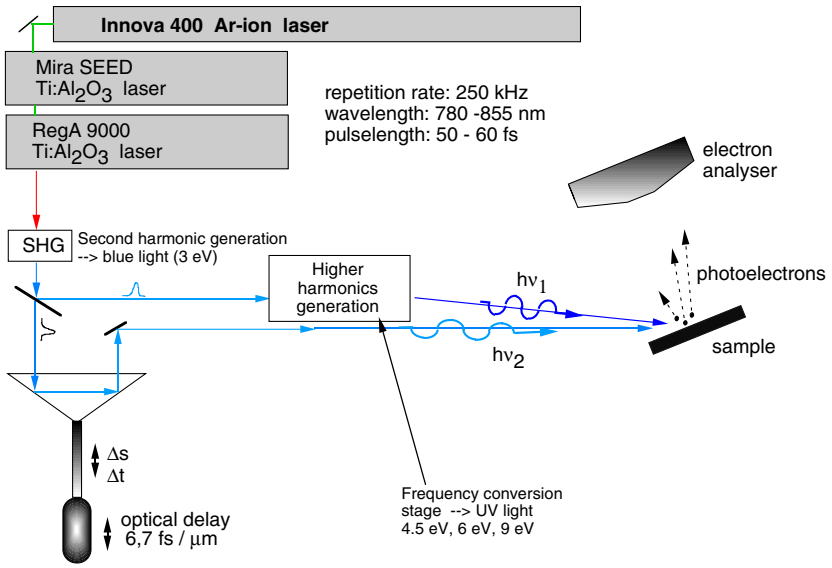

Figure 3. The infrared laser radiation is frequency doubled and split into two parts. The reflected light is again frequency converted (⇒UV light), while the other part could be delayed in time using a retroreflector. The two beams are focused onto the same spot of the sample, which is mounted in a vacuum chamber.

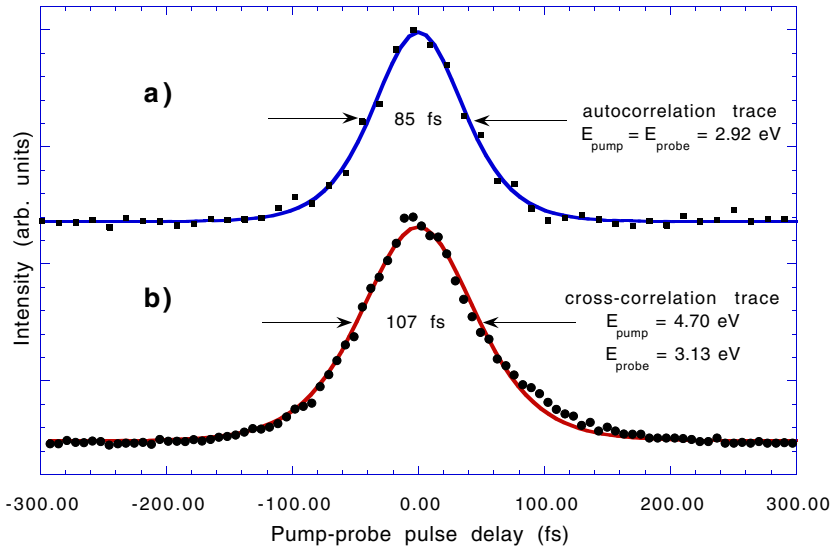

Figure 4. (a) The autocorrelation curve of a blue-laser pulse with a duration of 55 fs. (b) The cross-correlation curve in a two-colour experiment ($\hbar\omega_{\mathrm{pump}} = 4.7$ eV, $\hbar\omega_{\mathrm{probe}} = 3.13$ eV). The corresponding fits are based on a sech^2 function.

pump-and-probe pulses is scanned, the pulse length can be extracted from the temporal response of the 2PPE signal. An autocorrelation trace of second-harmonic light pulses with a photon energy of 2.92 eV is shown in figure 4(a) (solid squares). These data exhibit a peak-to-background ratio close to the expected value of 3:1. The full width at half-maximum (FWHM)

is deduced to be 85 fs by fitting a $\mathrm{sech}^2(t) = (\exp(1.76t/\tau)+\exp(-1.76t/\tau))^{-2}$ function (solid line) to the data. A sech^2 pulse shape describes the pulse shape better than other functions, e.g. a Gaussian. Deconvolution of the sech^2 fit results in a duration of 55 fs for the second-harmonic laser pulse. Similarly, the pulse length of 4.5 eV and 3 eV photons can be obtained. An example is shown in figure 4(b).

3. Examples: electronic relaxation in solids

In solids the electronic levels are occupied up to the Fermi level. The dynamics of excited electrons is strongly affected by the detailed electronic structure. In metals, electrons populating previously unoccupied states can decay very rapidly by exciting electron–hole pairs. This mechanism is blocked in semiconductors. Conduction electrons can, therefore, exhibit much longer lifetimes which is of great interest for semiconductor device technology.

Excited electron dynamics can be probed by TR2PPE spectroscopy. In this case electrons are first excited into unoccupied states by absorption of a photon. Their population dynamics is subsequently studied in a photoemission process using a second photon. In this section we will describe two examples of TR2PPE experiments on semiconductors and metals.

3.1. fs time-resolved photoemission of C_{60}

C_{60} has attracted attention as a non-linear medium for frequency conversion [13], as photoconducting material [14] and in photovoltaic applications [15]. It can be easily deposited onto solid substrates. In the following we will describe the investigation of a 20 nm thick C_{60} film evaporated onto a metal substrate [16, 17]. Occupied and unoccupied electronic energy levels were probed by 2PPE at various photon energies. The results are summarized in figure 5.

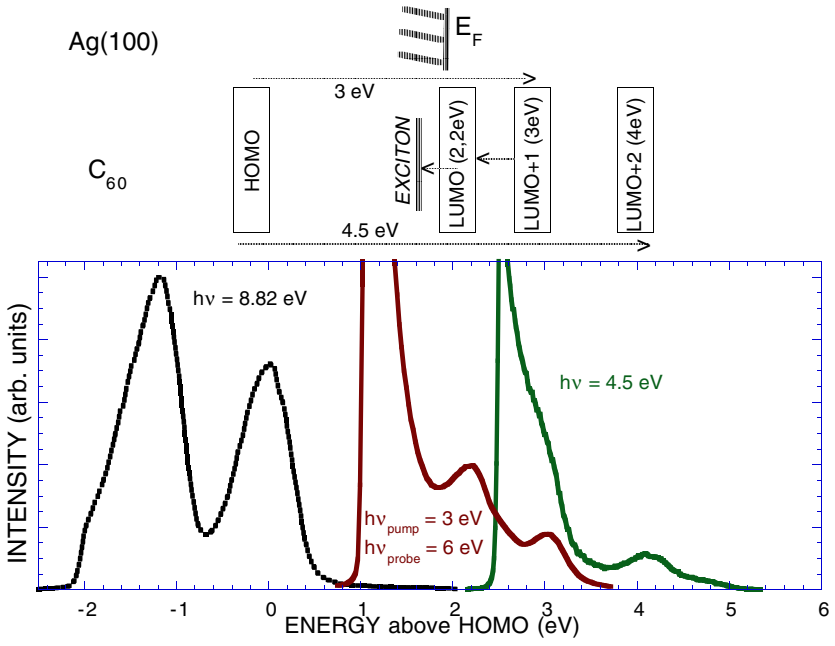

Figure 5. Occupied and unoccupied orbitals of C_{60}, obtained with various photon energies.

The occupied valence energy levels were determined using a photon energy of 8.82 eV. Two peaks are clearly visible which correspond to the two highest-lying occupied states HOMO − 1 and HOMO (highest occupied molecular orbital) of the C_{60} molecule with energies of −2.18 and −3.4 eV relative to the Fermi level, respectively. An optical transition between the HOMO and the lowest unoccupied molecular orbital (LUMO) is dipole forbidden. In order to populate the LUMO with electrons, a photon energy of 3 eV is used. It is well known that C_{60} shows strong photon absorption in this energy range. To probe the excited electron distribution caused by 3 eV pump photons, the fourth harmonic of 6 eV photon energy was used. With the two beams in spatial and temporal overlap on the sample, two features next to the vacuum cut-off in the energy distribution curve (EDC) can be observed in figure 5. The peak at 2.3 eV (closest to E_F) above the HOMO is attributed to electrons occupying the LUMO and the second peak at 3 eV is attributed to electrons occupying the next higher state, LUMO + 1. The EDC on the right in figure 5 was obtained with a photon energy of 4.5 eV. Since the ionization potential exceeds 4.5 eV, photoemission can only occur via resonant two-photon excitation due to absorption of two photons by the same electron. There are again two features visible. The peak next to the vacuum cut-off is again caused by electrons populating LUMO + 1 while a new feature, due to occupation of the next-higher-lying energy band, LUMO + 2, appears at 4 eV above the HOMO.

The population dynamics of C_{60} is shown in figure 6 where a series of TR2PPE spectra are displayed, taken with different time delays between the pump (3 eV) and probe pulses (6 eV). All energy positions of the excited states are referenced to the centre of the HOMO.

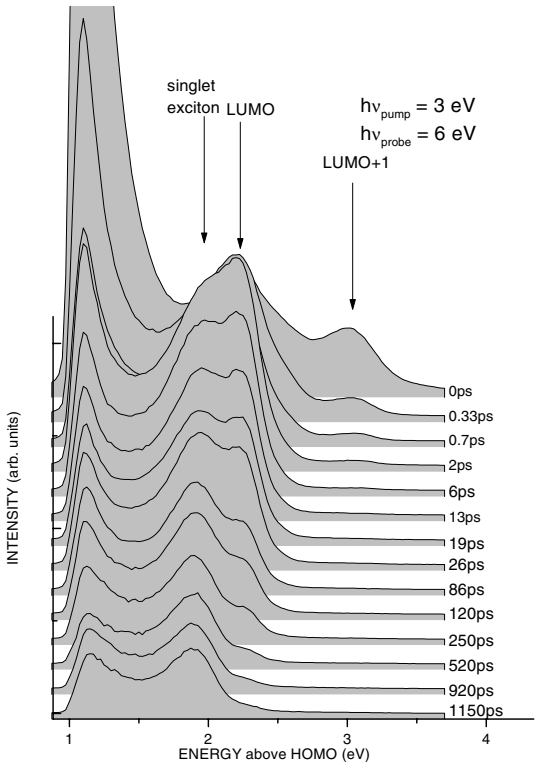

Figure 6. Temporal evolution of the excited electronic population of a 20 nm thick C_{60} layer on a metal substrate.

The structures at 2.3 eV and 3 eV above the HOMO have already been mentioned. The peak at 1.9 eV becomes visible only long after excitation and is, therefore, not discernible in figure 5 ($\Delta t = 0$ ps). This peak has a different origin to the other structures and is attributed to the singlet exciton. It can clearly be seen that these states relax with different timescales. Here it should only be mentioned that LUMO + 1 decays with a relaxation time of about 300 ± 35 fs while the deeper-lying states such as LUMO (130 ± 30 ps) and the singlet exciton (1 ± 0.1 ns) decay on much longer timescales.

3.2. Image-potential-state dynamics on Pt(111)

A class of surface states which are of particular interest arise when electrons are bound to metallic surfaces by their own image charges. Such electrons are repeatedly reflected between the crystal and the image barrier. The image-potential states are pinned to the vacuum level and form a Rydberg series of discrete energy levels with binding energies $E_B = 0.85\,\text{eV}/(n + \Delta)^2$ converging towards the vacuum level [18]. The quantum defect Δ is related to the phase shift for a reflection at the crystal surface and has values $0 \leqslant \Delta \leqslant 0.5$. A major ingredient in the formation of image-potential states is a high electron reflectivity at the crystal surface for energies just below the vacuum level. These image-potential states are theoretically well understood and provide a model system for studying excited electron dynamics at metal surfaces.

Figure 7 shows a series of typical 2PPE spectra probing the image-potential-state population on the clean Pt(111) surface [19, 20]. The first two image-potential states, $n = 1$ and $n = 2$, can be resolved with binding energies of 0.65 ± 0.03 eV and 0.16 ± 0.03 eV respectively. Figure 7 also shows that with increasing delay time between the pump and probe pulses the relative intensity between the two image-potential states changes. At a delay time of 340 fs only the $n = 2$ image-potential state is still occupied while the $n = 1$ state is already completely depopulated. These observations demonstrate qualitatively a longer lifetime of the second image-potential state. Another effect seen in the spectra especially for the $n = 2$ state

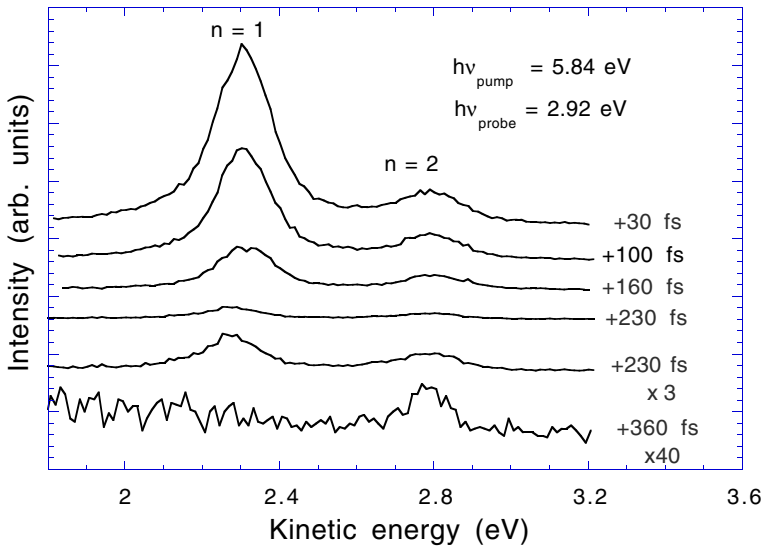

Figure 7. Energy distribution curves of the image-potential states at different times after excitation.

is the decrease of the spectral width with increasing delay time. The broadening at short delay times can be attributed to direct two-photon ionization which can only occur when the two pulses are in temporal overlap.

We determined the image-potential-state lifetimes from the cross-correlation traces shown in figure 8. The energy analyser was set to the kinetic energy values of the emitted photoelectrons corresponding to the image-potential-state peaks in figure 7 while the pump–probe pulse delay was scanned (solid symbols). The instrumental cross-correlation function was obtained from photoemitted electrons of an intermediate state 3 eV above E_F on the unprepared Pt(111) sample (open squares). On this surface all image-potential states are quenched and no lifetime effects were observed. The full width at half-maximum of the cross-correlation trace was deduced to be 152 fs by fitting a sech^2 function (solid lines) to the data (open squares). We determined the probe pulse duration to be 60 fs separately; thus, the temporal resolution is mostly limited by the pump pulse width. The transient responses of the image-potential states are affected by lifetime effects in two different ways [12]. The maximum of the transient response of the first image-potential state is shifted 14 fs towards positive delay time. In addition the curve is slightly broadened by 18 fs. Both effects can be seen (solid lines and symbols) by comparing the data to the cross-correlation trace (dashed lines). A far stronger effect is seen in the transient response of the $n = 2$ state. The curve becomes significantly broader and shows an asymmetric shape due to the longer lifetime of this state.

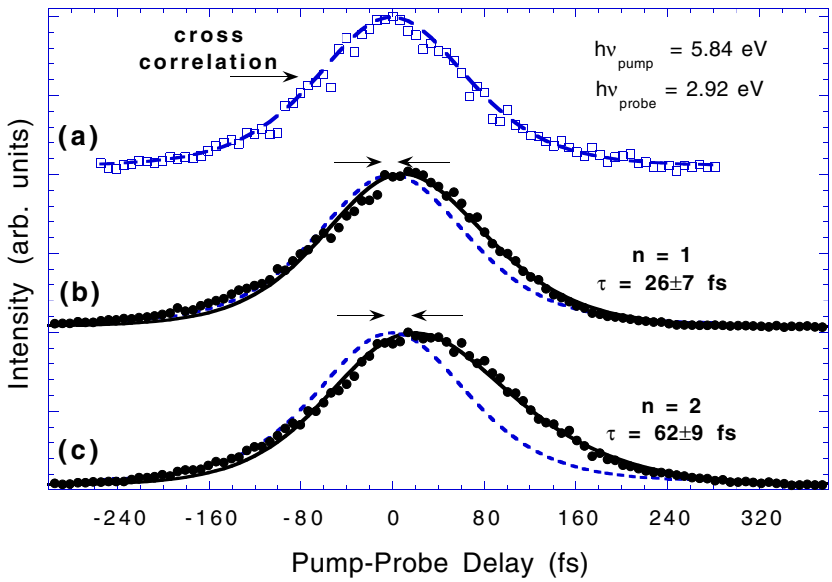

Figure 8. Transient responses of the $n = 1$ (middle panel) and $n = 2$ (bottom panel) image-potential states (solid symbols). The cross-correlation trace (open squares) displayed in the top panel reflects the instrumental function described by a sech^2 function (dashed lines). From fits of a rate equation model (solid lines) to the data, lifetimes of 26 ± 7 fs and 62 ± 7 fs were obtained for the $n = 1$ state and $n = 2$ state, respectively.

4. Summary

Pump–probe measurements with fs laser pulses allow us to probe dynamical processes on the shortest experimentally controllable timescales. We have given an overview of the state-

of-the-art laser technology and demonstrated the scope of the method for two examples. The transient population of unoccupied states is strongly affected by materials properties. In metals, lifetimes of only several fs are observed, while for semiconductors, excited electrons can show lifetimes up to ns. Other applications of fs pump–probe experiments could not be described here. For instance, it is now possible to observe chemical reactions in real time as well as to trigger and influence them. This flexibility of fs spectroscopy opens up a wide field for further applications in the future.

References

[1] Petek H and Ogawa S 1997 *Prog. Surf. Sci.* **56** 239
[2] Aeschlimann M, Bauer M, Pawlik S, Weber W, Burgermeister R, Oberli D and Siegmann H C 1997 *Phys. Rev. Lett.* **79** 5158
[3] Nisoli M, De Silvestri S, Svelto O, Sartania S, Cheng Z, Lenzner M, Spielmann Ch and Krausz F 1997 *Appl. Phys.* B **65** 189
[4] *Mira Model Seed, Operator's Manual* 1999 COHERENT Laser Group, Santa Clara, CA 95054
[5] Bechthold P S 2000 Ultrashort light pulses: generation, handling, detection *31. Ferienkurs des Instituts für Festkörperforschung des Forschungszentrums Jülich* ed Th Brückel and W Eberhardt
[6] Bor Zs and Racz B 1985 *Opt. Commun.* **54** 165
[7] Borsutzky A, Brünger R, Huang Ch and Wallenstein R 1991 *Appl. Phys.* B **52** 55
Borsutzky A, Brünger R and Wallenstein R 1991 *Appl. Phys.* B **52** 380
[8] Hilbig R, Hilber G and Wallenstein R 1986 *Appl. Phys.* B **41** 225
[9] Nebel A and Beigang R 1991 *Opt. Lett.* **16** 1729
[10] Hertel T, Knoesel E, Wolf M and Ertl G 1996 *Phys. Rev. Lett.* **76** 535
[11] Höfer U, Shumay I L, Reuß Ch, Thomann U, Wallauer W and Fauster Th 1997 *Science* **277** 1480
[12] Knoesel E, Hertel T, Wolf M and Ertl G 1995 *Chem. Phys. Lett.* **240** 409
[13] Kuhnke K, Becker R and Kern K 1996 *Chem. Phys. Lett.* **257** 569
[14] Kazaoui S, Ross R and Minami N 1995 *Phys. Rev.* B **52** 11 665
[15] Yu G, Gao J, Hummelen J C, Wudl F and Heeger A J 1995 *Science* **270** 1789
[16] Jacquemin R, Kraus S and Eberhardt W 1998 *Solid State Commun.* **105** 449
[17] Link S, Scholl A, Jacquemin R and Eberhardt W 2000 *Solid State Commun.* **113** 689
[18] Fauster Th 1994 *Appl. Phys.* A **59** 479
[19] Link S, Dürr H A and Eberhardt W 2000 *Appl. Phys.* A **71** 525
[20] Link S, Dürr H A, Bihlmayer G, Blügel S, Eberhardt W, Chulkov E V, Silkin V M and Echenique P M 2001 *Phys. Rev.* B **63**